

Spin state of Mn^{2+} and magnetism in vanadate-carbonate compound, $\text{K}_2\text{Mn}_3(\text{VO}_4)_2\text{CO}_3$

Kartik Samanta and T. Saha-Dasgupta

Department of Condensed Matter Physics and Materials Science S. N. Bose National Centre for Basic Sciences, Kolkata 700098, India

(Received 30 October 2013; revised manuscript received 1 August 2014; published 21 August 2014)

The magnetic properties of vanadate-carbonate compound, $\text{K}_2\text{Mn}_3(\text{VO}_4)_2\text{CO}_3$, has been discussed in recent literature in terms of unusual low-spin configuration of Mn^{2+} . Using first-principles density functional theory-based microscopic analysis of electronic and magnetic structure of this compound, we find that contrary to previous suggestion, two inequivalent Mn^{2+} ions in this compound, one in octahedral and another in trigonal-bipyramidal coordination of oxygen atoms, are both in high-spin state. Our first-principles determination of Mn-Mn magnetic exchanges leads to a spin-5/2 model consisting of alternate layers of honeycomb and triangular spin lattices, with vastly differing strengths of magnetic interactions in the two layers, which are very weakly connected among themselves. The computed magnetic susceptibility and magnetization, based on the derived spin model, are compared with measured thermodynamic data.

DOI: [10.1103/PhysRevB.90.064420](https://doi.org/10.1103/PhysRevB.90.064420)

PACS number(s): 75.10.Jm, 75.30.Et, 71.20.-b

I. INTRODUCTION

Spin state when describing transition metal (TM) complexes is an important concept, which refers to spin configurations of the metal center's d electrons, given a specific charge state of it. In many of the cases, especially for transition metal ions with d occupancy between 4 and 7, spin states can vary between high-spin and low-spin configurations. At the molecular level, the stabilization of a specific spin state depends primarily on the competition between the crystal field splitting and the Hund's rule coupling, the latter favoring high-spin (HS) configuration, through maximization of total spin, and the former favoring low-spin (LS) configuration, as the high-spin configuration involves transfer of electron from lower energy states to higher energy states [1]. While the Hund's rule coupling energy is a characteristic energy of the transition metal ion and therefore shows only mild variation, the crystal field splitting depends on the period (row in periodic table) of the TM ion, the charge of the metal ion, and the field strength of the complex's ligands. The first two factors are fixed for a choice of a given TM and for a given composition. However, the last factor remains flexible and can be modulated by changing the local environment of the TM ion. Such spin state transitions, by change in local environment of TM ions through external perturbation, are well known in literature. For example, in case of metalorganic polymers, comprising of TM centers, usually Fe^{2+} , linked through organic ligands, the ligand field strength has been modulated through application of temperature, pressure, or light irradiation, triggering spin crossover [2]. The other well-known example is the example of cobaltites, particularly for Co^{3+} ions, which can exist in low-spin, high-spin, as well as intermediate spin state [3]. The temperature-dependent spin-state transition in prototype Co(III) system, LaCoO_3 , is a topic of discussion [4].

Following the above knowledge, one may expect Mn^{2+} ion with d^5 configuration to exist in two possible spin states, the high-spin state with $S = 5/2$ state and low-spin state with $S = 1/2$ state. The existence of low-spin state of Mn^{2+} , though, is unexpected due to the large Hund's rule stabilization, arising from half-filled d shell. It is, therefore, a debatable issue, whether Mn^{2+} ion can exhibit spin-state bistability, as commonly observed [5] in the case of Fe^{2+} or Co^{3+} .

There exists only a handful of reports of low-spin state of Mn^{2+} in ambient condition, e.g., Mn substituted RuS_2 and RuSe_2 [6], and tris (quinone oximates) of Mn(II, III) [7]. The first vanadate-carbonate compound, $\text{K}_2\text{Mn}_3(\text{VO}_4)_2\text{CO}_3$, with Mn^{2+} ions, was synthesized employing hydrothermal synthesis [8], which provided the opportunity of creating two different local environments of Mn^{2+} within the same compound, one in octahedral surrounding of oxygen atoms (Mn1) and another in trigonal-bipyramidal environment of oxygen atoms (Mn2). The magnetic susceptibility was measured and the data was explained in terms of the high-spin state and low-spin state of Mn1 and Mn2, respectively, in two different local environments in the compound. The proposal of the low-spin state of Mn^{2+} in $\text{K}_2\text{Mn}_3(\text{VO}_4)_2\text{CO}_3$ is curious given the very few known examples of LS Mn^{2+} . An independent theoretical investigation, based on first-principles calculations, will therefore be a worthwhile task. The literature on successful application of first-principles calculation to derive the underlying spin model on a microscopic basis, given a compound, is growing [9], resulting in an established confidence in this approach. Also, the geometry of the magnetic Mn^{2+} ions offered by the crystal structure of the compound is fascinating due to the possible effect of frustration [10].

In the present study, we carry out density functional theory (DFT) [11] calculations to examine the proposal of low-spin state of Mn^{2+} in $\text{K}_2\text{Mn}_3(\text{VO}_4)_2\text{CO}_3$. We further employ two independent methods: (a) Wannier function-based derivation of a low-energy model Hamiltonian [12], constructed out of full DFT electronic structure and subsequent application of super-exchange formula, and (b) DFT total energy calculation of various magnetic arrangements, to determine the underlying spin model [13]. This derived spin model is then solved by Monte Carlo technique [14] to compute the thermodynamic properties, such as magnetic susceptibility and magnetic field dependence of the magnetization, which are compared with the measured data. Our study reveals that contrary to the conclusion drawn from the experimental study, both Mn sites in two different crystallographic environments in the compound are in high-spin $S = 5/2$ state. Application of super-exchange and total-energy methods gives rise to two very similar descriptions of the underlying $S = 5/2$ spin model. The derived spin model comprises a dominant nearest-neighbor interaction between

Mn1 ions forming honeycomb lattice, along with small but nonnegligible values of further neighbor interactions, an order of magnitude smaller nearest-neighbor interaction between Mn2 ions forming triangular lattice, compared to that in Mn1 layer, and a tiny interaction between Mn1 and Mn2. The calculated thermodynamic properties are found to provide description of the measured data. The conclusions, drawn based on our theoretical study, may be verified in terms of future experiment, like a neutron-scattering experiment.

II. COMPUTATIONAL METHOD

For the DFT calculations, we have used two different basis sets: (a) the muffin-tin orbital (MTO)-based linear muffin-tin orbital (LMTO) [15] method and the N th-order MTO method, namely, NMTO method [12] as implemented in the STUTTGART code; (b) the plane-wave-based basis as implemented in the Vienna *ab initio* simulation package (VASP) [16]. The NMTO method, which relies on self-consistent potential generated by the LMTO method, has been used for deriving the low-energy Hamiltonian defined in the basis of effective Mn- d Wannier functions, by integrating out the degrees of freedom related to K, V, C, and O. The real-space representation of the low-energy Hamiltonian provides the information of crystal field splitting at inequivalent Mn sites as well as effective hopping interactions between two Mn sites. The energetically accurate plane-wave basis set calculation have been employed to calculate the total energy of different spin configurations to derive the magnetic exchanges from the total-energy method. The consistency between the calculations in two basis sets has been checked in terms of band structure, density of states, magnetic moments, etc. We have also cross-checked our results in terms of full potential linear augmented plane wave (LAPW) basis set calculations, especially in connection with the spin-polarized results, determining the spin states of Mn. The exchange-correlation functional for the self-consistent calculations was chosen to be that of generalized gradient approximation (GGA) implemented following the Perdew-Burke-Ernzerhof prescription [17]. To check the missing correlation energy at Mn sites beyond GGA, calculations with supplemented Hubbard U (GGA + U) were carried out, with choice of $U = 4$ eV and $J_H = 0.8$ eV. For the self-consistent field calculations in plane-wave basis, energy cutoff of 500 eV, and $6 \times 6 \times 2$ Monkhorst-Pack k -points mesh were found to provide a good convergence of the total energy. We considered a $1 \times 2 \times 1$ supercell and a $2 \times 6 \times 4$ Monkhorst-Pack k -point mesh, for the total-energy calculations of various different spin configurations. For LAPW calculations, we chose the APW + lo as the basis set and the expansion in spherical harmonics for the radial wave functions was taken up to $l = 10$. The charge densities and potentials were represented by spherical harmonics up to $l = 6$. The commonly used criterion for the convergence of basis set, relating the plane wave cutoff, K_{\max} and the smallest atomic sphere radius, R_{MT} , $R_{\text{MT}} * K_{\max}$ was chosen to be 7.0. The thermodynamic properties like magnetic susceptibility and magnetization were calculated by considering the *ab initio*-derived spin model on a $20 \times 20 \times 10$ lattice, by using Monte Carlo technique. The Monte Carlo code, as implemented in package within

Algorithms and Libraries for Physics Simulations project [14], for quantum spin models with arbitrary spin size and magnetic field, was used.

III. CRYSTAL STRUCTURE

The crystal structure of $\text{K}_2\text{Mn}_3(\text{VO}_4)_2\text{CO}_3$ may be considered as derivative of $\text{BaNi}_2(\text{VO}_4)_2$ -type structure [18]. The basic structural units [8] are composed of VO_4 tetrahedra, CO_3 triangle, Mn_2O_5 trigonal-bipyramid, and Mn_1O_6 edge-sharing octahedral units, as shown in Fig. 1(a). The two different polyhedral environment of Mn ions gives rise to two inequivalent Mn ions in the unit cell, Mn1 and Mn2, which form two types of layers, shown in Fig. 1(b). The neighboring Mn_1O_6 octahedra share edges to form honeycomb layer of Mn1 ions, shown in the bottom panel of the Fig. 1(b), while Mn_2O_5 trigonal bipyramids are connected to each other via CO_3 triangles, forming a triangular layer, shown in the top panel of Fig. 1(b). These two layers alternate along the c axis, as shown in Fig. 1(c), which are connected via VO_4 tetrahedra through sharing of oxygen vertices's with Mn polyhedra, to form the three-dimensional structure. The K^+ ions, not shown in the figure for clarity, sit in the crisscross channels formed in the structure and bring cohesion to the structure.

Starting from the experimentally determined structure, we carried out structural optimization in a plane-wave basis calculation within non-spin-polarized GGA setup, keeping the hexagonal $\text{P6}_3/\text{m}$ symmetry of the cell as well as lattice parameters fixed at experimentally determined values [8]. During the optimization, the positions of the atoms were relaxed toward equilibrium until the Hellman-Feynman force became less than 0.01 eV/Å. The comparison of the atomic positions in the optimized structure with that of the experimentally determined structure may be found in the table in Appendix A. As is evident from the table, the changes upon structural relaxation are not significant. The Mn-O bondlengths are found to show a reduction of only 1–2 % upon optimization, compared to experimentally measured structure. The results reported in the following are based on the theoretically optimized structure. Calculations have been cross-checked considering the experimentally measured structure too. This is been found to keep the general conclusions unchanged (cf. for example results presented in Table I).

IV. RESULT

A. DFT Electronic structure and spin state of Mn^{2+}

The DFT results for the electronic structure of the compound, as calculated in the framework of GGA in plane-wave basis, are summarized in Fig. 2. The non-spin-polarized density of states projected onto Mn1- d states, Mn2- d states, V- d states, O- p states, and C states are shown in Fig. 2(a). We notice that the states close to Fermi level, ϵ_F (set at zero in the figure) are dominated by Mn1- d and Mn2- d states, which are half-filled, in agreement with nominal Mn^{2+} valence with d^5 configuration. The Mn1- d and Mn2- d states are found to be hybridized with O- p states, as expected, but also shows nonnegligible hybridization with V- d states. The inset of the figure shows the zoomed plot, which shows this hybridization even clearly. Small but finite hybridization

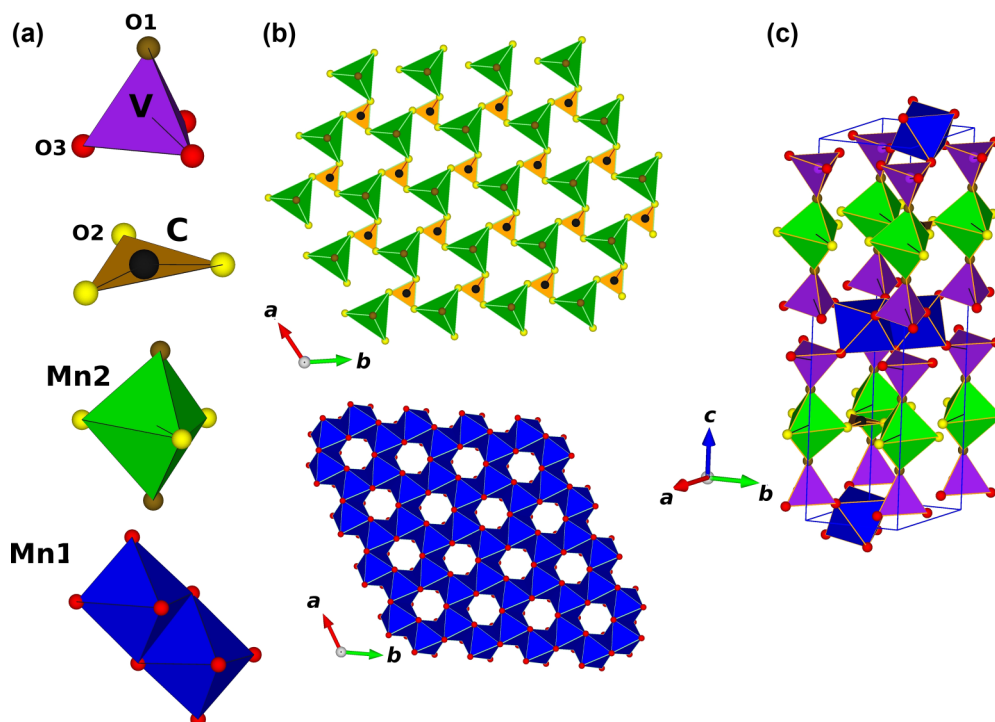


FIG. 1. (Color online) Crystal structure of $\text{K}_2\text{Mn}_3(\text{VO}_4)_2\text{CO}_3$. (a) The basic structural units, VO_4 , CO_3 , Mn_2O_5 , and edge-sharing Mn_1O_6 octahedra (from top to bottom). The inequivalent oxygens have been marked. (b) The layered sublattices of Mn_1 (bottom panel) and Mn_2 (top panel). (c) The connected, three-dimensional network.

from $C-p$ states is also observed. Figures 2(b) and 2(c) show the spin-projected density of states of Mn_1-d and Mn_2-d , respectively, as given by spin-polarized GGA calculation. The calculated magnetic moments are shown in Table I. In order to check the influence of the crystal structure, the magnetic moments calculated for the experimental crystal structure are also shown for comparison. To check the influence of strong correlation effect at Mn site, additionally GGA + U calculations have been performed for both the structures. As found from Table I, both the optimized as well as experimental crystal structure give rise to high-spin states of Mn_1 and Mn_2 (with moment values of 4.3–4.6 μ_B), both at level of GGA as well as GGA + U calculation ($U = 4$ eV and $J_H = 0.8$ eV). As expected, application of supplemented U, is found to increase the magnetic moments at Mn sites (by ≈ 0.2 μ_B). The total moment in the two-formula unit cell was found to

TABLE I. Magnetic moment at V, Mn_1 , Mn_2 , and inequivalent O sites (in μ_B) as calculated in GGA and GGA + U, considering measured as well as theoretically optimized crystal structures. The moment at C sites being vanishingly small has not been shown.

	Measured Structure		Optimized Structure	
	GGA	GGA + U	GGA	GGA + U
V	0.367	0.251	0.490	0.388
Mn_1	4.346	4.550	4.276	4.510
Mn_2	4.408	4.585	4.366	4.561
O1	0.003	0.001	0.003	0.002
O2	0.012	0.005	0.008	0.003
O3	0.036	0.018	0.031	0.011

be 30 μ_B corresponding to a moment of 5 μ_B per Mn. The rest of the moment is found to reside at O and largely at V site (~ 0.3 – 0.5 μ_B), stressing once again the importance of the hybridization with V- d states. In order to check the robustness of our conclusion about the HS state of Mn_2 , which is in apparent contradiction with experimental suggestion, we checked the influence of the initial guess by starting with LS state of Mn_1 and Mn_2 , which converged to HS state solution for both Mn_1 and Mn_2 . We also checked the influence of the basis set by carrying out calculations in full potential all electron LAPW method [19], in addition to LMTO and plane wave calculations. Calculations in all three basis sets gave rise to same conclusion of HS state of both Mn_1 and Mn_2 .

We further carried out fixed-moment calculations, constraining the total moment, which encompasses various possible spin states of Mn, by varying the total moment over a wide range within both GGA and GGA + U calculation setup. The obtained results are shown in Fig. 3. We find in both for GGA as well as GGA + U calculations, the minimum energy is obtained at a total magnetic moment of 30 μ_B , which corresponds to HS state of Mn_1 and Mn_2 , considering 4 Mn_1 atoms and 2 Mn_2 atoms in the unit cell. The choice of LS state of Mn_2 and HS state of Mn_1 , amounting to a total magnetic moment of 22 μ_B in the unit cell, or the LS states of both Mn, amounting to a total magnetic moment of 6 μ_B , are clearly not the ground-state energy configurations.

In order to rationalize the high-spin configuration of Mn_1 and Mn_2 , we computed the energy-level diagram of Mn- d states by NMTO-downfolding procedure [12] of constructing Mn- d only Hamiltonian out of a non-spin-polarized GGA self-consistent band structure, by integrating out all other

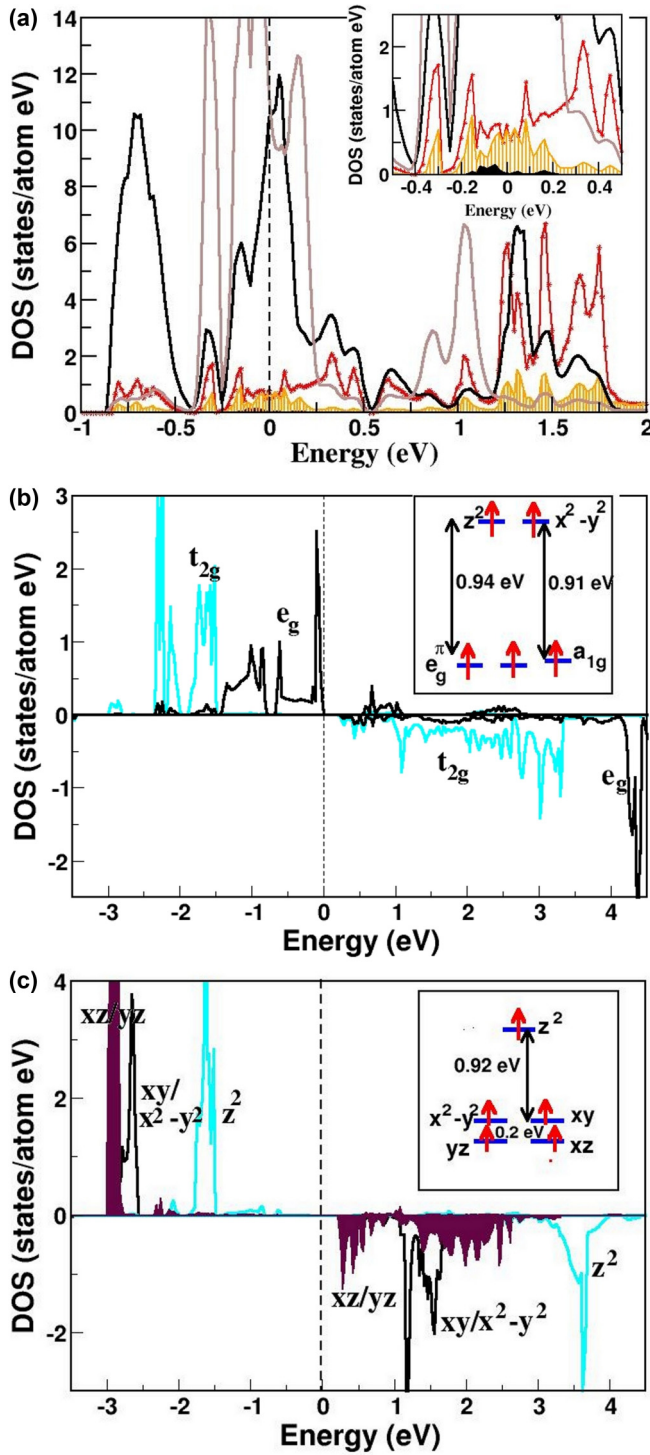


FIG. 2. (Color online) (a) Non-spin-polarized GGA density of states, projected onto Mn1- d (black, solid line), Mn2- d (brown/light gray, solid line), O- p (orange/gray-shaded area), V- d (red/dark gray, solid line), and C- p (black, shaded area). The zero of the energy is set at GGA Fermi energy. Inset shows the zoomed plot of the same. (b) Spin-polarized GGA density of states, projected onto octahedral crystal field split Mn1- t_{2g} and Mn1- e_g states. Inset shows the energy level positions of Mn1- d states and their occupancies. The distortion in Mn1O₆ octahedra gives rise to small splitting within t_{2g} states. (c) Spin-polarized GGA density of states, projected onto crystal field split Mn2- d states. Inset shows the energy-level positions of Mn2- d states and their occupancies.

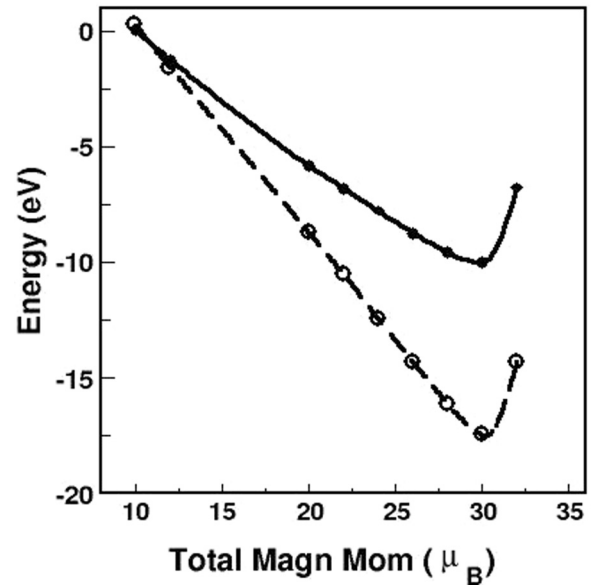


FIG. 3. Energy plotted as a function of the fixed total magnetic moment in the unit cell, consisting of four Mn1 and two Mn2 ions. The solid and dashed lines correspond to calculations within GGA and GGA + U, respectively.

degrees of freedom other than Mn- d . The onsite matrix elements of the real-space representation of this Hamiltonian provide us with the information of crystal field splitting of d states of Mn1 and Mn2 sites. The energy-level diagrams, shown as insets in Figs. 2(b) and 2(c), show t_{2g} - e_g splitting in the almost perfect octahedral environment of Mn1 with splitting of ~ 0.9 eV, and a splitting into double degenerate xz/yz , doubly degenerate $(x^2-y^2)/xy$, and singly degenerate $3z^2-r^2$ for the trigonal-bipyramidal environment of Mn2 with a splitting of ~ 0.9 eV between $3z^2-r^2$ and the next-lower-energy level. Considering the splitting of ~ 0.9 eV between the highest energy state and the next-lower-energy state, comparable to Hund's exchange, the high-spin states of Mn2, as in Mn1, are conceivable, supporting the calculated values of magnetic moments.

We note that $S = 1/2$ state for Mn2 would lead to Jahn-Teller active configuration with the unpaired spin residing at doubly degenerate $d_{x^2-y^2}/d_{xy}$ level, leading to distortion of crystal lattice. While the experimental study assigns the anomaly at $T \approx 83$ K to be tentatively of Jahn-Teller origin, the same study also reports no indication of this distortion is seen in specific heat measurements [8], making the situation rather undecided. This signature is also not found in the crystal structure data.

B. Evaluation of magnetic interactions

Next, we attempt on finding the magnetic interaction between the Mn²⁺ ions. For this purpose, we followed two independent routes. In the first approach, the low-energy Mn- d -only Hamiltonian out of the non-spin-polarized DFT band structure, was constructed by NMTO-downfolding procedure [12], by keeping only Mn1- d and Mn2- d degrees of freedom active, and integrating out the rest. The downfolded Mn- d -only bands in comparison to non-spin-polarized DFT band

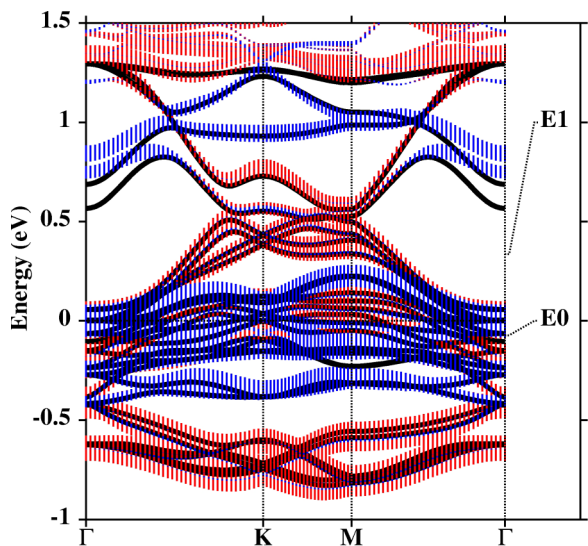


FIG. 4. (Color online) NMTO downfolded Mn- d only bands, shown in black, solid lines, in comparison to Mn1- d (the fatness, shown as red, vertical lines) and Mn2- d (the fatness, shown as blue, vertical lines) projected states of the full band structure.

structure projected onto Mn1- d and Mn2- d characters are shown in Fig. 4. This energy-selective procedure is capable of producing a faithful representation of the Mn- d -dominated bands, which are overlapping with other bands in high-energies and therefore challenging. The low-energy Mn- d -only Hamiltonian is defined in the basis of effective Mn- d Wannier functions, which has the central part shaped according to the d symmetries, while the tails, sitting at neighboring sites, are shaped according to the symmetries of integrated-out degrees of freedom, such as O- p , V- d , C- p , etc. The real-space representation of this low-energy Hamiltonian provides the onsite energies of the effective Mn- d levels, as presented in the insets of Fig. 2, as well as the effective hopping interactions connecting two Mn sites. The strongest interaction turned out to be that connecting nearest-neighbor (NN) Mn1 sites in the Mn1 layer, t_1 , followed by two more, second and third NN interactions in the Mn1 layer, t_2 and t_3 . The interactions

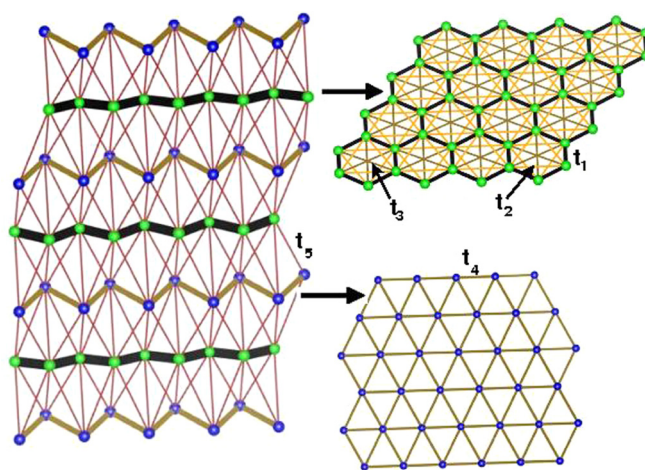


FIG. 5. (Color online) The dominant Mn-Mn effective hopping interactions, in the Mn1 layer (right top), Mn2 layer (right bottom), and that between Mn1 and Mn2 layers (left). The Mn1 and Mn2 sites are shown as green (light gray) and blue (dark gray) balls, respectively. The fatness of the connecting bonds, connecting two sites, are proportional to the corresponding hopping strength.

connecting NN Mn2 sites in Mn2 layer (t_4) are found to be nonnegligible but smaller than the strongest Mn1-Mn1 NN hopping interaction. The hopping connecting Mn1 and Mn2 (t_5) between the two layers is found to be small. The dominant effective Mn-Mn hopping interactions in the sublattice of Mn ions are shown in Fig. 5. The values of the hopping interactions between different Mn- d orbitals, sitting at sites i and j , as given by NMTO-downfolding, may be found in Appendix B. From the knowledge of hopping interaction $t_{m,m'}^{ij}$, where i and j are two Mn sites and m and m' are two d orbitals, and the energy-level difference, $\Delta_{m,m'}^{ij}$, between m and m' orbitals at sites i and j , we employ the super exchange formula [20], $\sum_{m,m'} \frac{2(t_{m,m'}^{ij})^2}{\Delta_{m,m'}^{ij} + U}$, to compute the magnetic exchanges, J . The antiferromagnetic (AFM) exchanges in terms of the strongest Mn1-Mn1 NN interaction, J_1 , turned out to be $\frac{J_2}{J_1} = 0.12$, $\frac{J_3}{J_1} = 0.06$, $\frac{J_4}{J_1} = 0.06$, $\frac{J_5}{J_1} = 0.04$, where J_2, J_3, J_4, J_5 represent second NN

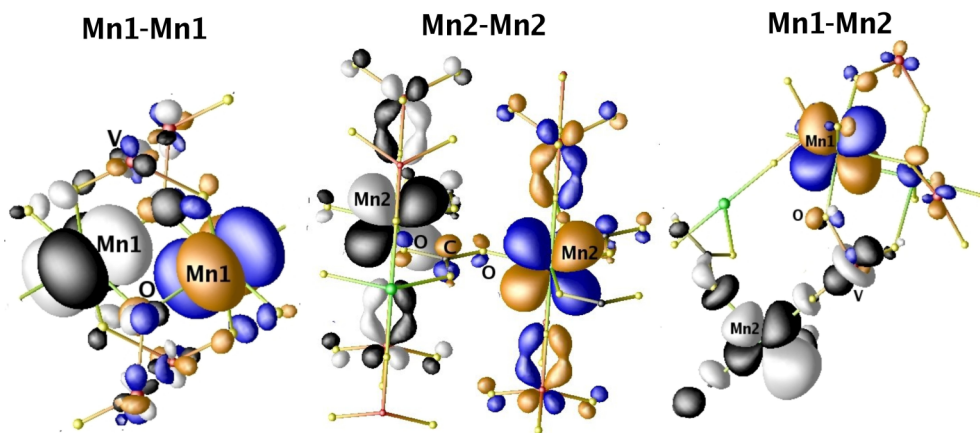


FIG. 6. (Color online) Mn1 and Mn2 Wannier functions placed at two interacting Mn sites. The two oppositely signed lobes of the wavefunctions at site $i(j)$ are colored differently as black (cyan/light gray) and white (orange/dark gray). From left to right, the plots show the cases for two Mn1 sitting at NN positions, two Mn2 sitting at NN positions, and Mn1 and Mn2 sitting at two adjacent layers.

Mn1-Mn1, third NN Mn1-Mn1, NN Mn2-Mn2, and Mn1-Mn2 interactions, respectively, with a choice of $U = 4$ eV.

In order to probe the underlying super-exchange path, we plot in Fig. 6 the Mn- d Wannier functions placed at two interacting Mn sites, corresponding to the strongest Mn1-Mn1 NN interaction, the Mn2-Mn2 NN interaction, and Mn1-Mn2 interaction between the two adjacent layers (from left to right). We find that Mn1-Mn1 NN interaction proceed not only through the edge-shared oxygens but also through the V sites, which bridge two Mn1 sites and contributes to Mn1-Mn1 interaction due to nonnegligible hybridization between V- d and Mn- d . Mn2-Mn2 interaction proceeds via the Mn-O-C-O-Mn super exchange paths, while the rather weak Mn1-Mn2 interaction between two adjacent layers is mediated by O-V-O path.

While the above analysis is based on the perturbative super-exchange formula, the alternative more accurate approach can be calculation of total energies for different magnetic arrangement of Mn spins and mapping onto the underlying Heisenberg model,

$$H = J_1 \sum_{nn} S_{Mn1}^i S_{Mn1}^j + J_2 \sum_{2nn} S_{Mn1}^i S_{Mn1}^j + J_3 \sum_{3nn} S_{Mn1}^i S_{Mn1}^j + J_4 \sum_{nn} S_{Mn2}^i S_{Mn2}^j + J_5 \sum_{nn} S_{Mn1}^i S_{Mn2}^j$$

to extract various J 's [13]. For this purpose, we constructed a supercell of dimension $1 \times 2 \times 1$, giving rise to 12 Mn atoms in the unit cell, which are labeled as shown in Fig. 7. The least-square-fitting procedure of the calculated GGA + U energies of different spin configurations (refer to Table II for the considered configurations and the energies) to the above defined Heisenberg model gave the estimate of J_1 , J_2 ,

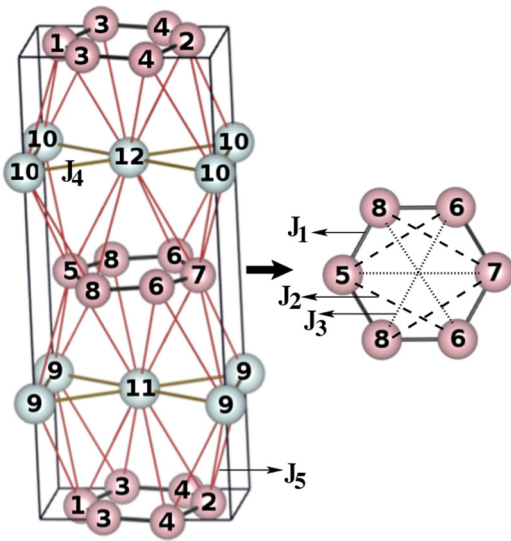


FIG. 7. (Color online) Labeling of Mn1 and Mn2 sites, forming alternate layers in the $1 \times 2 \times 1$ supercell, considered for total-energy calculations. The Mn1 and Mn2 atoms are colored differently as pink (dark gray) and light gray, respectively. The connections corresponding to J_1 , J_2 , J_3 , J_4 , and J_5 are indicated.

TABLE II. Magnetic configurations of the Mn ions in the supercell for the states used to determine the magnetic interactions. The numbering of the Mn sites are as shown in Fig. 7. The last column gives the relative GGA + U energies in eV.

	1	2	3	4	5	6	7	8	9	10	11	12	ΔE
FM	+	+	+	+	+	+	+	+	+	+	+	+	0.000
AFM1	+	-	-	+	+	+	-	-	+	+	+	+	-0.629
AFM2	+	-	+	-	+	-	+	-	+	+	+	+	-0.365
AFM3	+	-	+	-	+	+	-	-	+	+	+	+	-0.445
AFM4	+	+	+	+	+	+	+	+	+	+	-	-	-0.013
AFM5	-	-	-	-	-	-	-	-	+	+	+	+	-0.003
AFM6	-	+	+	-	+	+	-	-	-	-	+	+	-0.641
AFM7	+	-	+	-	-	+	-	+	-	+	+	-	-0.377
AFM8	+	-	+	-	-	+	+	-	+	-	+	-	-0.262
AFM9	+	+	+	+	+	+	+	+	+	-	+	+	-0.006
AFM10	-	-	-	-	-	-	-	-	+	-	+	-	-0.002
AFM11	+	+	-	-	-	-	-	-	-	+	-	+	-0.236
AFM12	+	-	+	-	+	-	-	+	-	-	-	+	-0.268
AFM13	+	+	+	+	-	-	-	-	-	-	-	+	-0.007
AFM14	+	-	+	+	+	+	+	-	+	+	+	+	-0.340
AFM15	+	-	+	+	+	+	+	-	+	-	+	-	-0.342

J_3 , J_4 , J_5 as -4.162 ± 0.033 meV, -0.242 ± 0.008 meV, -0.481 ± 0.130 meV, -0.123 ± 0.007 meV, and -0.005 ± 0.001 meV, respectively. Negative signs imply all interactions to be of antiferromagnetic nature. We find that total energy method gave rise to very similar description of the underlying spin model, as found in a super-exchange method, with a dominant J_1 in the Mn1 layer, small but nonnegligible values of J_2 and J_3 , a J_4 in Mn2 layer, which is less than order of magnitude smaller compared to J_1 , and a small interlayer coupling, J_5 . The value of J_5 is found to be smallest among all the interactions in both the approaches, indicating general agreement between the two approaches, although precise numerical values differ. The estimate of J_5 , as given in the total-energy method, turns out to be tiny, pushing it to the limit of DFT accuracy.

The above analysis leads to a spin-5/2 model consisting of alternate layers of honeycomb and triangular lattices, which are weakly connected to each other. The calculations, reported in the above, were carried out considering the collinear arrangement of the Mn spins. However, the frustration effect in the triangular geometry of the Mn2 spins is expected to lead to canting of the Mn spins with possible noncollinear arrangement. The classical phase diagram of possible ground-state magnetic structure for large S spins on a honeycomb

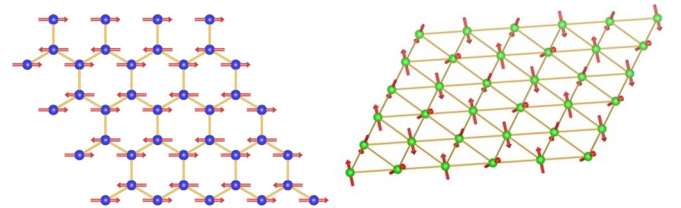


FIG. 8. (Color online) The lowest-energy spin structure of Mn spins, as given in DFT calculation, with Mn1 and Mn2 layers shown in left and right panels, respectively.

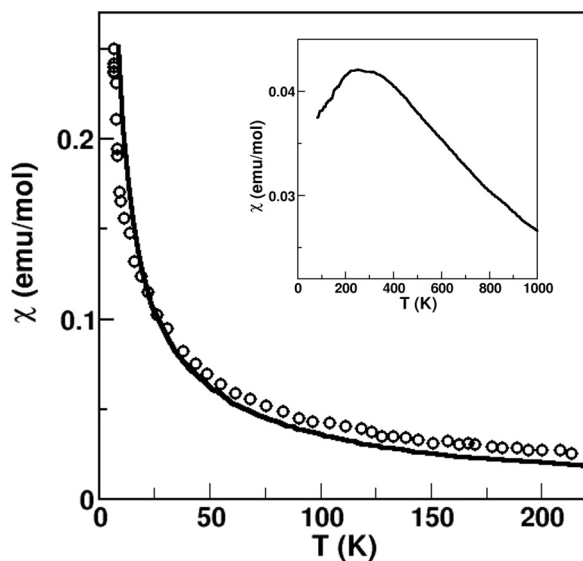


FIG. 9. Temperature dependence of magnetic susceptibility. The solid line and circle correspond to calculated susceptibility based on *ab initio*-derived spin model and experimental data [8], respectively. Inset shows the calculated susceptibility based on only Mn1-Mn1 interactions.

lattice, has been evaluated in literature for a J_1 - J_2 - J_3 model [21]. Following those structures, we find that the lowest-energy structure, as computed within GGA + U, to be noncollinear with 120° canting of spins in Mn2 layer of triangular lattice, and that in Mn1 layer to be collinear with alternate pointing of spins along the hexagonal ring of the honeycomb lattice, as shown in Fig. 8. The magnetic structure in Mn1 layer follows the expectation arising from a strong J_1 , and much weaker J_2 and J_3 , all being antiferromagnetic. The magnetic moments of the individual Mn spins in the noncollinear spin configuration were found to range between 4.6 and $4.8 \mu_B$, in good comparison to that found considering the collinear spin arrangement.

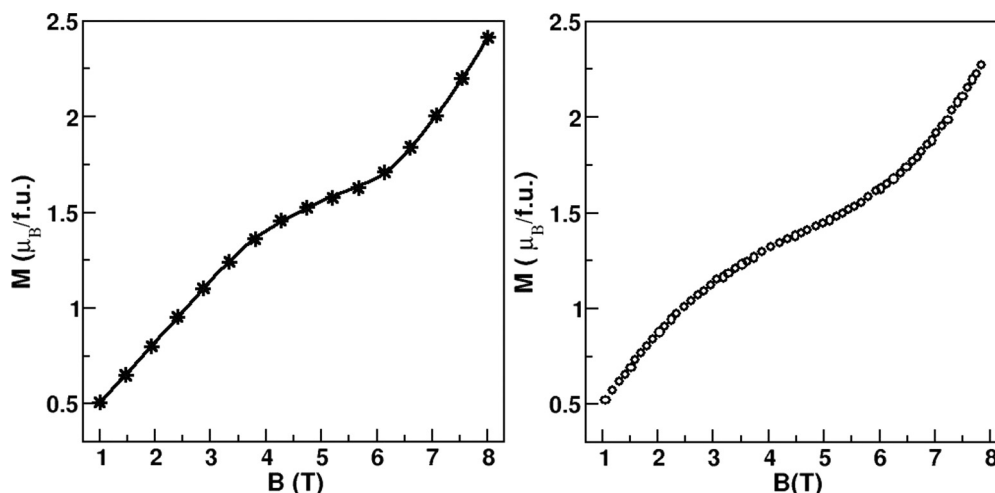


FIG. 10. The magnetic-field dependence of magnetization. The left and right panels correspond to calculation based on *ab initio*-derived spin model and experimental data [8], respectively. In the left panel, the stars mark the calculated data while the line is a spline fit through the data points.

C. Calculation of thermodynamic properties

Finally, we carried out the Monte Carlo simulation [14] of thermodynamic properties considering the *ab initio*-derived $S = 5/2$ spin model. Calculations have been carried out considering the J_1 - J_2 - J_3 - J_4 model, as effect of tiny J_5 is found to have negligible effect. The magnetic susceptibility as well as magnetization properties were calculated. In order to make the comparison of the theoretically computed susceptibility obtained from spin-spin correlation in presence of magnetic field of $B = 1T$, to that of the experimentally measured susceptibility (in [emu/mol]), the relation $\chi^{\text{exp}} = 0.5 S(S + 1)g^2 \chi^{\text{theory}}/J_1$ is used, where g denotes the Lande g factor, which has been fixed at experimentally determined value of 1.978 [8]. Note that g value being less than the free electron value of 2 is typical for Mn^{2+} ion in high-spin state. The theoretical result and the experimental data for magnetic susceptibility are presented in Fig. 9. The inset shows the calculated susceptibility considering only J_1 , J_2 , and J_3 , i.e., the interactions in Mn1-layer. In absence of interaction at the Mn2 layer, namely J_4 , the computed susceptibility shows a drop in low-temperature range, which changes drastically upon introduction of Mn2-Mn2 interaction. The overall agreement with the experimental data is moderately reasonable, given the uncertainties both in experimental measurement as well as in the various levels of approximations in the theoretical evaluation of the magnetic exchanges. Finally, we computed the magnetization as a function of varying magnetic field, at a temperature of 3 K, which is found to reproduce the initial fast rise, with slow rise at intermediate field value as well as a fast upturn at higher field value as observed experimentally, as shown in Fig. 10.

V. SUMMARY

Using first-principles density functional theory-based calculations, we investigate the proposal of low-spin configuration of Mn^{2+} ion in $\text{K}_2\text{Mn}_3(\text{VO}_4)_2\text{CO}_3$. The existence of low-spin configuration of Mn^{2+} at ambient condition is rare due to large Hund's rule energy gain and, therefore, this suggestion is

provoking. Our rigorous first-principles calculation establishes that, contrary to the previous suggestion, both inequivalent Mn^{2+} ions, Mn1 and Mn2, one in octahedral and another in trigonal-bipyramidal coordination, are in high-spin state. This is justified considering a crystal field splitting of ≈ 0.9 eV at both inequivalent Mn sites. Computation of magnetic exchanges employing Wannier function-based super-exchange formula, as well as mapping of total energies of different magnetic arrangements to Heisenberg model, establishes an antiferromagnetic $S = 5/2$ spin model of alternating layers of honeycomb and triangular lattices, which are coupled very weakly. The nearest-neighbor interaction in the honeycomb Mn1 layer is found to be the strongest interaction, followed by second- and third-neighbor interactions, in decreasing order, which are small but nonnegligible. The nearest-neighbor interaction in triangular Mn2 layer is found to be much smaller than that in Mn1 layer, setting the low-energy scale at which ordering takes place. The connection between Mn1 and Mn2 layers is very small and found to have negligible effect. The frustration effect in triangular lattice is found to give rise to noncollinearity with 120° canting of spins in Mn2 layer, and that in Mn1 layer is found to be collinear with alternate pointing of spins along the hexagonal ring of the honeycomb lattice, following the expectation from a dominant antiferromagnetic nearest neighbor, and small values of antiferromagnetic second- and third-nearest-neighbor interactions of large spins on a honeycomb lattice [21]. Solving the first-principles-derived spin model using Monte Carlo technique, we calculate the temperature dependence of magnetic susceptibility and the magnetic-field dependence of the magnetization, which were found to provide reasonable description of the experimental results. The difference in conclusion of the present study and the experimental study [8] concerning the spin state of Mn2

demands further experimental study on this interesting issue. Specifically, the suggestion [8] of the LS state of Mn2 should be reflected in its signature of Jahn-Teller activity, which is found in neither crystal structure data nor in specific heat data. We hope that our theoretical study will stimulate further experimental activity on this compound.

ACKNOWLEDGMENTS

The authors thank the Department of Science and Technology, India, for support through the Thematic Unit of Excellence and Unit for Nanoscience and Technology. The authors thank A. Vasiliev for bringing the problem into notice.

APPENDIX A

TABLE III. The theoretically optimized atomic positions compared to the experimentally measured data. During the optimization the parameters of the hexagonal unit cell are fixed at the experimentally measured values, $a = 5.21\text{\AA}$ and $c = 20.41\text{\AA}$.

Atom	Measured			Optimized		
	x	y	z	x	y	z
V	0.00000	0.00000	0.07987	0.00000	0.00000	0.07949
Mn1	0.66667	0.33333	0.00457	0.66666	0.33333	0.00427
Mn2	0.00000	0.00000	0.25000	0.00000	0.00000	0.25000
K	0.33333	0.66667	0.15776	0.33333	0.66666	0.15759
C	0.66667	0.33333	0.25000	0.66666	0.33333	0.25000
O1	0.00000	0.00000	0.15520	0.00000	0.00000	0.15626
O2	0.44340	0.06810	0.25000	0.43342	0.06483	0.25000
O3	0.30980	0.98939	0.05494	0.31628	0.99217	0.05337

APPENDIX B

TABLE IV. Effective hopping interactions (in eV) between two Mn sites which can be either Mn1 or Mn2 (see third column), connected through the connecting vector, as given in the first column, and separated by a distance, as given in the fourth column of the table. The number of neighbors for a given pair of Mn sites is indicated in the second column. Each hopping interaction is a 5×5 matrix, $h_{m,m'}$ with $m, m' = d_{xy}, d_{yz}, d_{3z^2-1}, d_{xz}$, and $d_{x^2-y^2}$.

Connecting vector hopping int.	NN no.	Atoms	Distance (\AA)	d_{xy}	d_{yz}	d_{3z^2-1}	d_{xz}	$d_{x^2-y^2}$	
[0.58 0.00 - 0.04] t_1	3	Mn1-Mn1	3.01	d_{xy}	-0.057	-0.033	0.009	0.045	0.007
				d_{yz}	0.033	0.048	-0.023	-0.032	-0.009
				d_{3z^2-1}	-0.009	-0.023	-0.154	-0.023	-0.101
				d_{xz}	0.045	0.032	0.023	0.282	0.004
				$d_{x^2-y^2}$	-0.007	-0.009	-0.101	-0.004	-0.270
[0.00 - 1.00 0.00] t_2	6	Mn1-Mn1	5.20	d_{xy}	0.000	-0.014	-0.035	-0.015	0.047
				d_{yz}	-0.020	-0.016	0.013	-0.006	-0.028
				d_{3z^2-1}	0.026	-0.073	0.014	-0.012	-0.092
				d_{xz}	0.010	-0.003	-0.026	-0.003	-0.056
				$d_{x^2-y^2}$	-0.001	-0.001	0.016	-0.028	-0.014
[0.58 - 1.00 - 0.04] t_3	3	Mn1-Mn1	6.01	d_{xy}	-0.004	0.007	-0.050	-0.035	-0.010
				d_{yz}	-0.007	0.009	-0.001	0.021	-0.004
				d_{3z^2-1}	0.050	-0.001	-0.007	0.025	-0.021
				d_{xz}	-0.035	-0.021	-0.025	0.008	-0.027
				$d_{x^2-y^2}$	0.010	-0.004	-0.021	0.027	0.000

TABLE IV. (Continued.)

Connecting vector hopping int.	NN no.	Atoms	Distance (Å)		d_{xy}	d_{yz}	d_{3z^2-1}	d_{xz}	$d_{x^2-y^2}$
					d_{xy}	d_{yz}	d_{3z^2-1}	d_{xz}	$d_{x^2-y^2}$
[0.00 – 1.00 0.00]	6	Mn2-Mn2	5.20	d_{xy}	–0.003	0.000	–0.025	0.000	–0.040
t_4				d_{yz}	0.000	0.010	0.000	–0.004	0.000
				d_{3z^2-1}	–0.037	0.000	–0.031	0.000	0.005
				d_{xz}	0.000	0.040	0.000	–0.005	0.000
				$d_{x^2-y^2}$	–0.069	0.000	–0.037	0.000	–0.020
					d_{xy}	d_{yz}	d_{3z^2-1}	d_{xz}	$d_{x^2-y^2}$
[0.29 – 0.50 – 1.09]	6	Mn1-Mn2	6.35	d_{xy}	0.003	0.010	0.007	–0.000	0.001
t_5				d_{yz}	–0.006	0.018	–0.022	0.003	–0.023
				d_{3z^2-1}	0.021	0.013	–0.023	–0.001	–0.044
				d_{xz}	–0.009	–0.048	0.003	0.000	0.011
				$d_{x^2-y^2}$	0.000	–0.008	0.012	–0.002	0.012

- [1] H. L. Schlfer and G. Gliemann, *Basic Principles of Ligand Field Theory* (Wiley Interscience, New York, 1969).
- [2] P. Gtlich and H. A. Goodwin (Eds.), *Spin Crossover in Transition Metal Compounds, Top. Curr. Chem.* (Springer, Berlin, 2004), pp. 233–235; S. Brooker and J. A. Kitchen, *Dalton Trans.* **7331–7340** (2009).
- [3] H. Wu, *Phys. Rev. B* **86**, 075120 (2012); **81**, 115127 (2010); H. Wu and T. Burnus, *ibid.* **80**, 081105(R) (2009).
- [4] H. Hsu, P. Blaha, and R. M. Wentzcovitch, *Phys. Rev. B* **85**, 140404(R) (2012).
- [5] D. Chernyshov *et al.*, *Angew. Chem. Int. Ed* **42**, 3825 (2003); I. Krivokapic *et al.*, *Coord. Chem. Rev.* **251**, 364 (2007).
- [6] Y. Jiang-Tsui, H. Ying-Sheng, and L. Shoen-Sheng, *J. Phys.: Condens. Matter* **2**, 5587 (1990).
- [7] P. Basu and A. Chakravorty, *Inorg. Chem.* **31**, 4980 (1992).
- [8] O. V. Yakubovich, E. V. Yakovleva, A. N. Golovanov, A. S. Volkov, O. S. Volkova, E. A. Zvereva, O. V. Dimitrova, and A. N. Vasiliev, *Inorg. Chem.* **52**, 1538 (2013).
- [9] Soumyajit Sarkar, Sudipta Kanungo, and T. Saha-Dasgupta, *Phys. Rev. B* **82**, 235122 (2010); A. A. Tsirlin, A. Möller, B. Lorenz, Y. Skourski, and H. Rosner, *ibid.* **85**, 014401 (2012); O. Janson, A. A. Tsirlin, J. Sichelschmidt, Y. Skourski, F. Weickert, and H. Rosner, *ibid.* **83**, 094435 (2011).
- [10] A. P. Ramirez, *Annu. Rev. Mater. Sci.* **24**, 453 (1994).
- [11] W. Kohn and L. J. Sham, *Phys. Rev.* **140**, A1133 (1965).
- [12] O. K. Andersen and T. Saha-Dasgupta, *Phys. Rev. B* **62**, R16219 (2000).
- [13] C. S. Hellberg, W. E. Pickett, L. L. Boyer, H. T. Stokes, and M. J. Mehl, *J. Phys. Soc. Jpn.* **68**, 3489 (1999).
- [14] ALPS project (Algorithms and Libraries for Physics Simulations); A. W. Sandvik, *Phys. Rev. B* **59**, R14157(R) (1999); F. Alet, S. Wessel, and M. Troyer, *Phys. Rev. E* **71**, 036706 (2005); L. Pollet, S. M. A. Rombouts, K. Van Houcke, and K. Heyde, *ibid.* **70**, 056705 (2004).
- [15] O. K. Andersen and O. Jepsen, *Phys. Rev. B* **12**, 3060 (1975).
- [16] G. Kresse and J. Hafner, *Phys. Rev. B* **47**, 558(R) (1993); G. Kresse and J. Furthmuller, *ibid.* **54**, 11169 (1996).
- [17] J. P. Perdew, K. Burke, and M. Ernzerhof, *Phys. Rev. Lett.* **77**, 3865 (1996).
- [18] R. Wichmann and Hk. Muller-Buschbaum, *Rev. Chim. Miner.* **21**, 824 (1984).
- [19] P. Blaha, K. Schwartz, G. K. H. Madsen, D. Kvasnicka, and J. Luitz, *WIEN2K, An Augmented Plane Wave + Local Orbitals Program for Calculating Crystal Properties*, edited by K. Schwarz (Technische Universität Wien, Austria, 2001).
- [20] K. I. Kugel and D. I. Khomskii, *Sov. Phys. Usp.* **25**, 231 (1982).
- [21] J. B. Fouet, P. Sindzingre, and C. Lhuillier, *Eur. Phys. J. B* **20**, 241 (2001); E. Rastelli, A. Tassi, and L. Reatto, *Physica B* **97**, 1 (1979).